LETTERS

Radio-frequency scanning tunnelling microscopy

U. Kemiktarak[1], T. Ndukum[3], K. C. Schwab[3] & K. L. Ekinci[2]

The scanning tunnelling microscope (STM)[1] relies on localized electron tunnelling between a sharp probe tip and a conducting sample to attain atomic-scale spatial resolution. In the 25-year period since its invention, the STM has helped uncover a wealth of phenomena in diverse physical systems—ranging from semiconductors[2,3] to superconductors[4] to atomic and molecular nanosystems[5–9]. A severe limitation in scanning tunnelling microscopy is the low temporal resolution, originating from the diminished high-frequency response of the tunnel current readout circuitry. Here we overcome this limitation by measuring the reflection from a resonant inductor–capacitor circuit in which the tunnel junction is embedded, and demonstrate electronic bandwidths as high as 10 MHz. This ~100-fold bandwidth improvement on the state of the art translates into fast surface topography as well as delicate measurements in mesoscopic electronics and mechanics. Broadband noise measurements across the tunnel junction using this radio-frequency STM have allowed us to perform thermometry at the nanometre scale. Furthermore, we have detected high-frequency mechanical motion with a sensitivity approaching ~15 fm Hz$^{-1/2}$. This sensitivity is on par with the highest available from nanoscale optical and electrical displacement detection techniques, and the radio-frequency STM is expected to be capable of quantum-limited position measurements.

In typical STM operation, the tip is scanned over the sample surface, while keeping the tunnel resistance R_T constant in the range $1\,M\Omega \leq R_T \leq 1\,G\Omega$. The stray capacitance C_P in the macroscopic wiring limits the bandwidth, in most cases, to $1/2\pi R_T C_P \approx 10\,kHz$. This is far from the fundamental limit, I_T/e, which is the tunnelling rate of a single electron determined by its charge e. For a typical tunnel current $I_T \approx 1\,nA$, this suggests an available bandwidth of ~1 GHz. So far, researchers have demonstrated several avenues towards achieving better time resolution with the STM. Direct radio-frequency (RF) measurements on the tunnel current have shown signatures of electron spin resonance at high frequencies[10,11]. Using several amplifier stages instead of a single trans-impedance amplifier[12,13] improves the time resolution by roughly an order of magnitude, but with an undesirable reduction in the signal-to-noise ratio. Optically based pump-probe techniques[14,15], in rather complex experimental geometries, have allowed for picosecond time resolution in the tunnel current after long averaging times. Our approach here is to read out the tunnel junction resistance directly by engineering an inductor-capacitor (LC) impedance transformation network. Such impedance matching has been used to dramatically improve the read-out bandwidth and coupling efficiency of high impedance nanoscale devices such as single electron transistors[16], atomic point contacts[17] and nanomechanical resonators[18].

The essential components of the RF-STM are shown in the block diagram of Fig. 1a. The large tunnel junction resistance R_T is transformed down by an LC impedance transformation network, also called the tank circuit, which is coupled to a 50-Ω low-noise RF amplifier. In our implementation, the RF circuit is placed on a small circuit board and mounted in a variable temperature STM; it does not disturb the conventional low-frequency circuit of the STM (see Methods for a description of the apparatus). At the resonance frequency f_{LC} of the LC circuit, the total impedance becomes $Z_{RLC} = Z_{LC}^2/R_T$, where the inductance L and capacitance C determine Z_{LC}: $Z_{LC} = \sqrt{L/C}$. By engineering Z_{RLC} appropriately, one can couple the small changes in R_T efficiently into the high-frequency measurement circuit.

Figure 1b illustrates the underlying principle of RF-STM operation. The inset shows the reflected power from the resonant LC circuit at different R_T as a function of frequency, as the tip is lowered towards a flat region on a Au surface. The changes in R_T result in changes in the damping of the resonant LC circuit (made up of a 2 μH chip-inductor and a 0.33 pF chip-capacitor), thereby changing the reflected power. The tip–sample capacitance is ~1 fF (ref. 19) and does not load the circuit. With additional stray capacitances on the circuit board, the tank circuit resonates at $f_{LC} \approx 115\,MHz$. The main panel of Fig. 1b shows the on-resonance amplitude of the reflection coefficient, $|\Gamma(f_{LC})|$, as a function of R_T; here $\Gamma(f_{LC}) = [Z_{RLC}(f_{LC}) - 50\,\Omega]/[Z_{RLC}(f_{LC}) + 50\,\Omega]$. In RF-STM operation, the displayed change in $|\Gamma(f_{LC})|$ with R_T, namely, with the tunnel gap z, provides transduction of displacements into electrical signals. An approximate $|\Gamma(f_{LC})|$ versus z calibration can be naively obtained (Fig. 1b, upper axis) by assuming point contact at $R_0 \approx 25\,k\Omega$ and an exponentially increasing tunnel resistance, $R_T \approx R_0 e^{2\kappa z}$. For the Au surface, $\kappa \approx 1\,Å^{-1}$ is obtained from further measurements (see below, and Supplementary Information section 2).

The most straightforward way to demonstrate fast imaging by the RF-STM is in the 'constant height' mode. Here, after reducing the STM feedback gain, RF power at frequency f_{LC} is launched towards the tip at each scan grid point; the reflected power is then measured (see Methods). Owing to the reduced feedback, surface height variations and the subsequent R_T variations result in contrasts in the reflected power image. Ideally, the minimum measurement time at each scan point is set by the 2-MHz bandwidth of the tank circuit (half-width at half-maximum, HWHM), and is ~0.1 μs. In practice, our measurement speed is limited by the kHz-range resonances of the STM tube scanner (see Methods for further discussion of bandwidth). Figure 1c and d show images of a 100 nm × 100 nm area of a Au-on-mica sample taken by constant-current STM and RF-STM, respectively. The ~2.3-Å step heights observed are close to those of single Au(111) steps[20]. The RF-STM image has negative contrast as compared to the constant-current STM image: the higher the feature on the surface, the smaller the R_T and hence, the smaller the reflected power.

To calibrate the RF circuit, we have used the shot noise in the tunnel current. In shot noise measurements, we remove the directional coupler and analyse the voltage fluctuations with a spectrum analyser (SA; Fig. 2a inset). The main panel of Fig. 2a shows a typical measurement of the shot noise power collected in the tank circuit. The first step in the calibration is the extraction of the tank circuit Q.

[1]Department of Physics, [2]Department of Aerospace and Mechanical Engineering, Boston University, Boston, Massachusetts 02215, USA. [3]Department of Physics, Cornell University, Ithaca, New York 14853, USA.

The spectral density S_I of the shot noise satisfies[21]

$$S_I = 2eI_T \coth \frac{eI_T R_T}{2k_B T} \quad (1)$$

This expression depends upon R_T, I_T and the absolute temperature T as well as the Boltzmann constant k_B and the electronic charge e. Measurement of S_I can be used to determine[22]: (1) the gain-bandwidth product (GBW) of the amplifier when $I_T R_T >> k_B T/e$; and (2) the noise injected by the circuit when $I_T R_T \approx 0$. Figure 2b demonstrates the calibration process carried out at two different R_T values at 77 K. After accounting for the excess noise and the GBW, the data are fitted by the function in equation (1) using $T = 77$ K.

Beyond calibration, shot noise in the tunnel current can be used for primary thermometry, where the extracted temperature is only a function of fundamental physical constants with no need for further calibration. Shot-noise-based primary thermometry was recently demonstrated in lithographic metallic tunnel junctions[22]. Here we extend this approach to nanometre-scale tunnel junctions using the RF-STM. In these experiments, we keep the tip–sample gap fixed and measure the shot noise power at three different bath temperatures, to which both the tip and the sample are anchored. Figure 2c displays the effect of temperature on the noise power in RF-STM measurements. After removing the GBW and the excess noise, the temperature can be extracted from fits to equation (1). The expected temperature dependence in Fig. 2c encourages us to propose thermal imaging based on an RF-STM. In such an endeavour, one could measure the shot noise as a function of position over a sample surface, where there are local temperature deviations from the bath temperature. A straightforward analysis (see Supplementary Information section 1 and Supplementary Fig. 1) shows that the measured 'effective' shot noise temperature becomes $T_{eff} \approx (T_T + T_S)/2$ when the tip and sample are at different respective temperatures T_T and T_S—thereby conveying information about the local temperature variations. We believe that the RF-STM, with its broad bandwidth and nanometre-scale spatial resolution, is particularly suited for rapid thermal imaging[23] of technologically important devices—for example, advanced semiconductor chips, where heat flow at the nanoscale is currently the limiting factor on density and clock speed. Our estimates suggest that, at 300 K, with a background noise of 70 K, a 100 pixel × 100 pixel thermal image with ~1 K temperature resolution should be achievable in ~100 s (see Methods and Supplementary Information section 1). The spatial resolution in such a measurement should be determined by the nanoscale tunnel junction area.

The RF-STM can be used as a local broadband displacement sensor with ultrahigh displacement sensitivity[24]—in theory, limited by quantum mechanics[25–27]. In order to demonstrate this, we have performed displacement measurements on two different systems: a flat Au sample shaken by a piezoelectric actuator, and a micromechanical

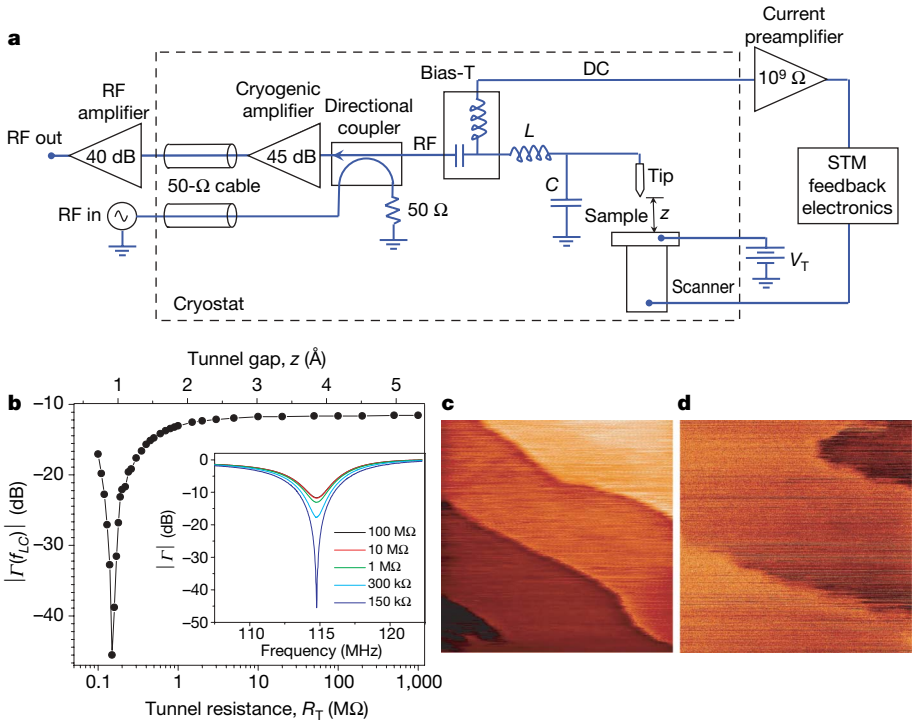

Figure 1 | Diagram and operation of the RF-STM. **a**, The tunnel junction is embedded in an *LC* tank circuit. Low-frequency tunnel current is separated from the RF signal and fed into the STM feedback circuit to control the tip–sample separation z. **b**, Reflection coefficient Γ as a function of tunnel junction resistance R_T on flame annealed Au deposited on mica. The inset shows Γ as a function of frequency at different R_T. At large R_T, the losses in the tank dominate the response; most of the incoming power is dissipated and the rest reflected. As R_T is reduced by bringing the tip closer to the surface, a better match to 50 Ω is obtained and the tank resonance-dip gets deeper, indicating more efficient RF power coupling to the tunnel junction. At $R_T \approx 150$ kΩ, best matching is achieved. Decreasing R_T further increases the impedance mismatch. Changes in Γ with R_T at the tank circuit resonance frequency, $f_{LC} \approx 115$ MHz (main panel), enable sensitive transduction of z into electrical signals. Starting from point contact ($R_0 \approx 25$ kΩ) and assuming an exponential decay $R_T \approx R_0 e^{2\kappa z}$ with $\kappa \approx 1$ Å^{-1}, a z calibration (top x-axis) is obtained. On this surface, the $\kappa \approx 1$ Å^{-1} value and the exponential dependence are verified experimentally for $R_T = 1$, 2 and 4 MΩ (see Supplementary Information section 2). The available bandwidth with this particular *LC* tank is ~2 MHz (HWHM). **c**, Constant-current STM image of 100 nm × 100 nm Au surface, showing several steps with height ~2.3 Å. Here, $R_T \approx 3$ MΩ, $I_T = 2$ nA and $V_T = 6$ mV. The scan speed is 1 s per line. A background was subtracted. **d**, RF-STM image of the same sample (at a different location) with $R_T \approx 4$ MΩ, $I_T = 2$ nA and $V_T = 8$ mV, and scan speed of 0.01 s per line. The scan area is again 100 nm × 100 nm. The displayed image is raw data. Because of the drifts and hysteresis in the scanner at high speeds, the exact same region shown in **c** could not be imaged. The RF-STM image has inverted contrast in comparison to the topography image. During imaging, the reduced feedback allows contrast to emerge at the step edges; then, feedback slowly attains the set d.c. tunnel current level on the terraces, reducing the contrast. The jump from a higher terrace to a lower one corresponding to an increase of ~2.3 Å results in a ~0.5 dB dip in the reflected power at $R_T \approx 4$ MΩ. All the data in this figure were acquired at room temperature.

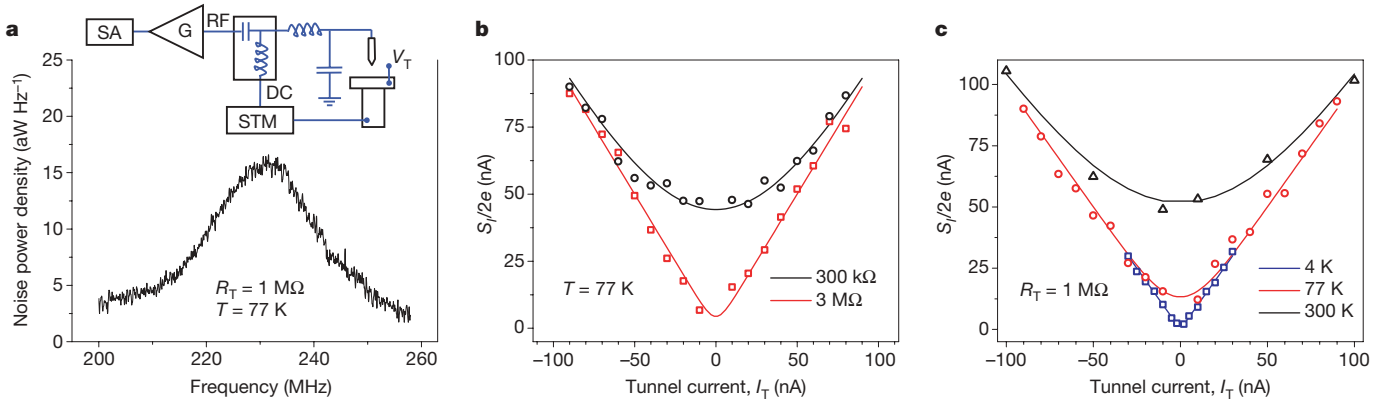

Figure 2 | Primary noise thermometry using the RF-STM. a, Typical RF noise power density at 77 K with $R_T \approx 1$ MΩ and $V_T = 200$ mV. Here, a different circuit made up of a 0.5 μH chip-inductor and a 0.5 pF chip-capacitor ($f_{LC} \approx 230$ MHz) enables a higher bandwidth of ~10 MHz (HWHM). The inset shows the simplified measurement schematic (SA, spectrum analyser; G, low-noise RF amplifier). **b**, Normalized shot noise power spectral density $S_I/2e$ at the tunnel junction displayed as a function of I_T at $R_T = 300$ kΩ and 3 MΩ. At the measurement temperature of 77 K, both measurements give an excess noise of ~35 K; the gain-bandwidth (GBW) product of the amplifier is $\sim 10^{11}$ Hz. **c**, $S_I/2e$ as a function of I_T at three different temperatures (300 K, 77 K and 4 K), but a fixed $R_T \approx 1$ MΩ. The continuous lines in **b** and **c** are fits to equation (1).

membrane excited at its resonant modes. Figure 3a and b respectively depict the simplified measurement set-up and a typical measurement obtained from this set-up. In the measurements, RF power at frequency f_{LC} is launched towards the tunnel junction, while the surface motion at frequency f_M modulates the reflected power. Data plotted in Fig. 3c are obtained from a collection of such reflection measurements on the Au surface as the surface oscillation amplitude Δz is increased. For small Δz, the sideband peak amplitude depends linearly on Δz. It is possible to obtain an estimate for the displacement sensitivity $\sqrt{S_z(f_M)}$ achievable by the RF-STM from this measurement. The spectral density $S_{V_r}(f_{LC} \pm f_M)$ of the RF voltage noise in the sideband limits the displacement sensitivity as

$$\sqrt{S_{V_r}(f_{LC} \pm f_M)} \approx \frac{V_c}{2} \left. \frac{\partial |\Gamma|}{\partial z} \right|_{R_T} \sqrt{S_z(f_M)} \qquad (2)$$

Here, V_c is the amplitude of the RF carrier at frequency f_{LC} and $\partial|\Gamma|/\partial z|_{R_T}$ represents the change in Γ with z around the bias point. Limited by the amplifier noise floor, we estimate $\sqrt{S_z} \approx 15\,\mathrm{fm\,Hz^{-1/2}}$ when $R_T \approx 1$ MΩ. The data in Fig. 3c in conjunction with the data in Fig. 1b also allow a direct measurement of the decay constant as $\kappa \approx 1\ \mathrm{Å}^{-1}$ (see Supplementary Information section 2).

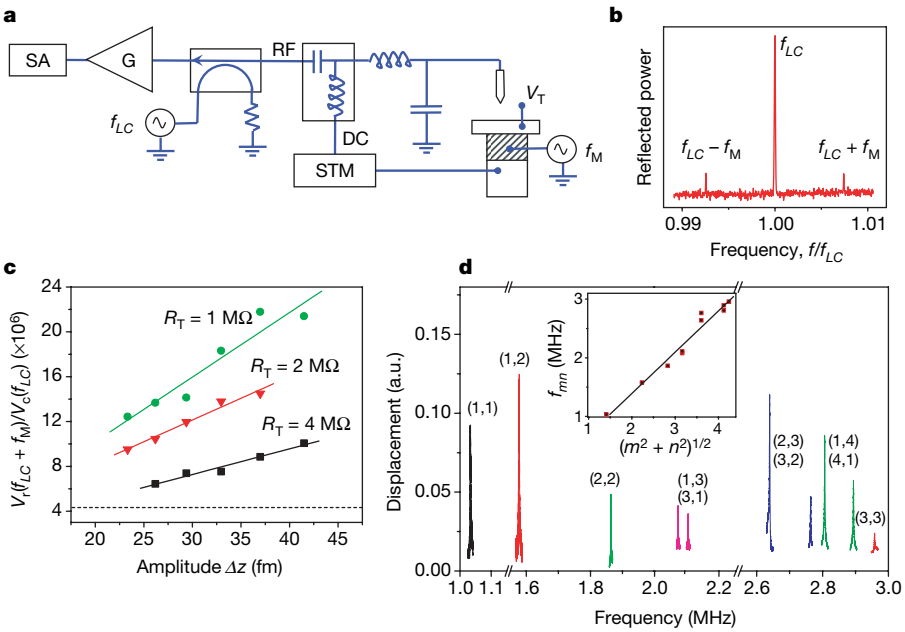

Figure 3 | RF-STM based displacement detection. a, The measurement set-up. **b**, A typical spectrum of the RF-STM signal when the tunnel gap z is modulated by the mechanical motion of the surface placed under the tip. The carrier signal is applied at frequency f_{LC} and the surface is moved at frequency f_M by a piezoelectric actuator (shaded), separate from the STM scanner. The circuit used in this experiment is identical to that in Fig. 1. Experiments are at room temperature. **c**, Displacement measurements on a flat Au surface. Each data point is the ratio of the single-sideband reflection amplitude $V_r(f_{LC} + f_M)$ to the carrier amplitude $V_c(f_{LC})$ plotted against the r.m.s. motion amplitude Δz at 1 MHz. A linear dependence of $V_r(f_{LC} + f_M)$ on Δz is observed at $R_T = 1$ MΩ, 2 MΩ and 4 MΩ, tunnel current $I_T = 2$ nA, and $V_c \approx 130$ μV. Linear fits to the data (solid lines) at each R_T go through the origin. The horizontal dashed line indicates the ~0.5 nV Hz$^{-1/2}$ noise floor set by the amplifier. The displacement sensitivity is obtained from the slope of each line; the best value (15 fm Hz$^{-1/2}$) is achieved at the lowest R_T. **d**, Swept frequency RF-STM measurements of the resonances of a micromechanical membrane. Here, the piezoelectric actuator is driven by a network analyser. The RF-STM signal is mixed-down with the carrier signal and is input into the detection port of the network analyser. The inset shows the measured eigenfrequencies as a function of mode number (m,n) of a membrane under tension. Note that the mode corresponding to $(n,m) = (2,1)$ is missing in the spectrum.

In a set of swept frequency measurements, we obtain the eigenmode frequencies of a membrane resonator (Fig. 3d). The micromechanical resonator is a ($w \times l \times t \approx 65\,\mu\text{m} \times 70\,\mu\text{m} \times 40\,\text{nm}$) silicon nitride membrane patterned with alignment marks and coated with a 25-nm-thick Au film (see Supplementary Information and Supplementary Fig. 3). In these measurements, the membrane motion is excited by the piezoelectric actuator; the RF-STM tip is positioned on a desired point on the moving membrane and the reflected power is monitored as a function of the drive frequency. The mode frequencies f_{mn} agree with optical interferometry measurements and accurately fit those of a membrane under tension, $f_{mn} \propto \sqrt{m^2 + n^2}$ (see Supplementary Information section 3)—as shown in Fig. 3d inset. Beyond displacement detection, this technique would be especially useful for imaging nanoscale motion. We also note that we observe back-action of the tip on the membrane motion (for example, due to electrostatic forces) resulting in perturbation of the observed mechanical parameters. Both mode imaging and back-action will be the subject of future work.

We expect the RF-STM to be applied to a number of important scientific and technological problems. The simplicity of the technique adds to its attractiveness: (1) relatively minor modifications to an existing STM are required; (2) the RF components are readily available; and (3) the RF circuit can work under a wide range of conditions, for example, in high vacuum, at low temperature, and in high magnetic field. From a microscopy point of view, a second-generation RF-STM, which could scan at speeds comparable to its augmented electronic bandwidth, would be the next step in development work[28]. A broadband STM controller circuit, which can feedback on the RF signal, would also be useful.

The RF-STM is well suited to the study of the dynamics of electronic phenomena with possibly atomic-scale resolution. An excellent example of this is the investigation of electron spin resonance. The tunnel current modulation at the Larmor precession frequency f_{ESR} of the electrons can be measured conveniently by a RF-STM. A direct way to detect narrowband ultrahigh-frequency current modulations at f_{ESR}, even with the current ~200 MHz tank frequencies, is to launch RF signals to the tunnel junction at $\sim f_{\text{ESR}} + f_{LC}$ and detect the modulation sideband at $\sim f_{LC}$. This approach is limited only by the typical tunnelling time for electrons. RF-STM-based shot noise measurements on exotic superconductors may enable the fast determination of quasi-particle nature[29].

Finally, electron tunnelling is expected to enable quantum-mechanically-limited position detection[25–27]. Research in this direction has begun to uncover interesting physics—in particular, the nature of back-action in detecting nanomechanical motion[17,30]. The RF-STM has the potential to further such studies, given that it is possible to tune the interaction strength and the position of the tip on the moving structure.

METHODS SUMMARY

The STM head design is a standard one, which comprises several piezoelectric elements. The head can be inserted into a continuous flow cryostat with a base temperature of 2.6 K. The STM-cryostat sits on an optical table for vibration isolation and can be pumped down to pressures below 1 torr. In the experiment, the tunnel bias voltage is connected to the sample. The *LC* network for transforming the tunnel junction resistance is attached to the STM tip; the rest of the circuit elements are placed on a small circuit board and are connected to the *LC* circuit embedding the tunnel junction. For imaging, the reflected power from the resonant circuit is detected using a homodyne power detector. In the shot noise measurements, the RF excitation arm of the circuit is removed and the homodyne detector is replaced with a spectrum analyser. In the displacement sensitivity measurements, the full circuit is used; the spectrum of the reflected signal is measured using a spectrum analyser. In the membrane mode measurements, swept frequency measurements are performed using a network analyser.

Full Methods and any associated references are available in the online version of the paper at www.nature.com/nature.

Received 19 April; accepted 7 September 2007.

1. Binning, G., Rohrer, H., Gerber, C. & Weibel, E. Surface studies by scanning tunneling microscopy. *Phys. Rev. Lett.* **49,** 57–61 (1982).
2. Stroscio, J. A., Feenstra, R. M. & Fein, A. P. Electronic structure of the Si(111)2 × 1 surface by scanning-tunneling microscopy. *Phys. Rev. Lett.* **57,** 2579–2582 (1986).
3. Wolkow, R. A. & Avouris, P. Atom-resolved surface chemistry using scanning tunneling microscopy. *Phys. Rev. Lett.* **60,** 1049–1052 (1988).
4. Pan, S. H. *et al.* Imaging the effects of individual zinc impurity atoms on superconductivity in $Bi_2Sr_2CaCu_2O_{8+\delta}$. *Nature* **403,** 746–750 (2000).
5. Eigler, D. M. & Schweizer, E. K. Positioning single atoms with a scanning tunnelling microscope. *Nature* **344,** 524–526 (1990).
6. Whitman, L. J., Stroscio, J. A., Dragoset, R. A. & Celotta, R. J. Manipulation of adsorbed atoms and creation of new structures on room-temperature surfaces with a scanning tunneling microscope. *Science* **251,** 1206–1210 (1991).
7. Manoharan, H. C., Lutz, C. P. & Eigler, D. M. Quantum mirages formed by coherent projection of electronic structure. *Nature* **403,** 512–515 (2000).
8. Hornbaker, D. J. *et al.* Mapping the one-dimensional electronic states of nanotube peapod structures. *Science* **295,** 828–831 (2002).
9. Madhavan, V., Chen, W., Jamneala, T., Crommie, M. F. & Wingreen, N. S. Tunneling into a single magnetic atom: spectroscopic evidence of the Kondo resonance. *Science* **280,** 567–569 (1998).
10. Manassen, Y., Hamers, R. J., Demuth, J. E. & Castellano, A. J. Jr. Direct observation of the precession of individual parametric spins on oxidized silicon surfaces. *Phys. Rev. Lett.* **62,** 2531–2534 (1989).
11. Durkan, C. & Welland, C. E. Electronic spin detection in molecules using scanning-tunneling-microscopy-assisted electron spin resonance. *Appl. Phys. Lett.* **80,** 458–460 (2002).
12. Mamin, H. J., Birk, H., Wimmer, P. & Rugar, D. High-speed scanning tunneling microscopy: Principles and applications. *J. Appl. Phys.* **75,** 161–168 (1994).
13. Rost, M. J. *et al.* Scanning probe microscopes go video rate and beyond. *Rev. Sci. Instrum.* **76,** 053710 (2005).
14. Nunes, G. & Freeman, M. R. Picosecond resolution in scanning tunneling microscopy. *Science* **262,** 1029–1032 (1993).
15. Weiss, S., Ogletree, D. F., Botkin, D., Salmeron, M. & Chemla, D. S. Ultrafast scanning probe microscopy. *Appl. Phys. Lett.* **63,** 2567–2569 (1993).
16. Schoelkopf, R. J., Wahlgren, P., Kozhevnikov, A. A., Delsing, P. & Prober, D. The radio-frequency single-electron transistor (RF-SET): A fast and ultrasensitive electrometer. *Science* **280,** 1238–1242 (1998).
17. Flowers-Jacobs, N. E., Schmidt, D. R. & Lehnert, K. W. Intrinsic noise properties of atomic point contact displacement detectors. *Phys. Rev. Lett.* **98,** 096804 (2007).
18. Truitt, P. A., Hertzberg, J. B., Huang, C. C., Ekinci, K. L. & Schwab, K. C. Efficient and sensitive capacitive readout of nanomechanical resonator arrays. *Nano Lett.* **7,** 120–126 (2007).
19. Kurokawa, S. & Sakai, A. Gap dependence of the tip-sample capacitance. *J. Appl. Phys.* **83,** 7416–7423 (1998).
20. Hallmark, V. M., Chiang, S., Rabolt, J. F., Swalen, J. D. & Wilson, R. J. Observation of atomic corrugation on Au(111) by scanning tunneling microscopy. *Phys. Rev. Lett.* **59,** 2879–2882 (1987).
21. Birk, H., de Jong, J. M. & Schönenberger, C. Shot-noise suppression in the single-electron tunneling regime. *Phys. Rev. Lett.* **75,** 1610–1613 (1995).
22. Spietz, L., Lehnert, K. W., Siddiqi, I. & Schoelkopf, R. J. Primary electronic thermometry using the shot noise of a tunnel junction. *Science* **300,** 1929–1932 (2003).
23. Majumdar, A., Carrejo, J. P. & Lai, J. Thermal imaging using the atomic force microscope. *Appl. Phys. Lett.* **62,** 2501–2503 (1993).
24. Binnig, G., Quate, C. F. & Gerber, Ch. Atomic force microscope. *Phys. Rev. Lett.* **56,** 930–933 (1986).
25. Yurke, B. & Kochanski, G. P. Momentum noise in vacuum tunneling transducers. *Phys. Rev. B* **41,** 8184–8194 (1990).
26. Presilla, C., Onofrio, R. & Bocko, M. F. Uncertainty-principle noise in vacuum-tunneling transducers. *Phys. Rev. B* **45,** 3735–3743 (1992).
27. Clerk, A. A. & Girvin, S. M. Shot noise of a tunnel junction displacement detector. *Phys. Rev. B* **70,** 121303 (2004).
28. Xu, Y., MacDonald, N. C. & Miller, S. A. Integrated micro-scanning tunneling microscope. *Appl. Phys. Lett.* **67,** 2305–2307 (1995).
29. Jehl, X., Sanquer, M., Calemczuk, R. & Mailly, D. Detection of doubled shot noise in short normal-metal/ superconductor junctions. *Nature* **405,** 50–53 (2000).
30. Naik, A. *et al.* Cooling a nanomechanical resonator with quantum back-action. *Nature* **443,** 193–197 (2006).

Supplementary Information is linked to the online version of the paper at www.nature.com/nature.

Acknowledgements We thank D. M. Karabacak for help with optical interferometry and A. Vandelay for discussions. This work was supported by the National Science Foundation through the Division of Materials Research (IMR Programme), the Division of Civil, Mechanical and Manufacturing Innovation (MDSE Programme) and the Cornell Center for Materials Research.

Author Information Reprints and permissions information is available at www.nature.com/reprints. Correspondence and requests for materials should be addressed to K.L.E. (ekinci@bu.edu).

METHODS

Apparatus. The STM head design is a standard one, which comprises several piezoelectric elements. The sample plate is attached to a central piezoelectric tube by a spring clip. The central tube is supported by three piezoelectric tubes and springs. The central tube can slide along the z-axis by 'slip-stick' motion resulting from the supporting piezos; moreover, the sample plate can be moved in the x–y plane by motion of the central piezo, thus enabling relative tip–sample motion along all three axes. The head is attached to the end of a 40-cm-long rod; this allows the insertion of the head into a continuous flow cryostat with a base temperature of 2.6 K. The STM-cryostat sits on an optical table for vibration isolation. The system can be pumped down to pressures below 1 torr. At room temperature, the experiments are either performed in an inert gas atmosphere or in vacuum. In cryogenic operation, the STM head is cooled by cold helium vapour, which flows from a liquid helium reservoir to the sample space through capillaries. The rate of this flow, and hence the base temperature, is controlled by a needle valve and a rotary pump.

In this experiment, the sample is connected to the tunnel bias voltage, while all the relevant RF and low-frequency circuitry are connected to the STM tip. The STM tip, a cut or etched Pt-Ir wire, is fixed onto a printed circuit board. This $\sim$2 cm $\times$ 2 cm board connects the tip to the LC tank circuit, the bias-T (Mini Circuits TCBT-2R5G) and the directional coupler (Mini Circuits DBTC-9-4+) as shown in Fig. 1a. The bias-T separates the low frequency part of the tunnelling signal from the high frequency part, and channels these two into the relevant circuits. The low frequency arm of the bias-T is connected to a current preamplifier by a coaxial cable $\sim$24 inches long. At the high frequency arm, there is a directional coupler that properly directs the incoming and reflected signals. After the directional coupler, there is a PCB to SMA connector, to which the low noise cryogenic RF amplifier (Miteq AFS3-00100200-09-CR-4) is connected. At room temperature, this amplifier has a gain of 45 dB and background noise temperature of $\sim$70 K. At 4 K, the gain goes up to 48 dB and the noise temperature goes down to $\sim$5 K. In the measurements, we used a second stage amplifier (Mini Circuits ZKL-1R5) outside the cryostat with a gain of 40 dB.

Imaging. For imaging, the RF reflectometry circuit in Fig. 1a is used after the addition of a homodyne power detector. First, feedback is reduced to its minimum value; this causes the tip to respond very slowly to surface height changes. A carrier signal at the resonance frequency f_{LC} of the LC circuit is launched towards the tunnel junction. As the STM tip scans over the surface, the surface corrugations result in changes in R_T due to the slow feedback; this, subsequently, changes the reflected power. The reflected RF power is mixed with the carrier at f_{LC} using a mixer (Mini Circuits ZP-3+). The baseband signal is digitized using an analogue-to-digital (A/D) converter and plotted on the scan grid points on a computer. In RF-STM imaging of the Au surface, the tank circuit has a bandwidth (HWHM) of $\sim$2 MHz. The IF bandwidth of the mixer is $\sim$400 MHz; the bandwidth of the A/D converter is $\sim$1 MHz. The factor that limits the current measurement speed is the kHz range resonant modes of the STM tube scanner.

Shot noise thermometry. In the shot noise measurements, the RF excitation arm of the circuit is removed and the homodyne detector is replaced with a spectrum analyser. As d.c. current is driven through the tunnel junction, the shot noise power is collected in the LC resonant circuit. This noise power is measured by a spectrum analyser. The averaging time for shot noise thermometry is obtained as follows: we take the background temperature as the sum of the ambient temperature, 300 K, and the noise temperature of our amplifier, 70 K: $T_{bg} \approx 370$ K. The measurement bandwidth is the bandwidth of the resonant tank circuit. In this experiment, the bandwidth is $B \approx 10$ MHz (HWHM) as shown in Fig. 2a. The averaging time τ to achieve $\Delta T \approx 1$ K temperature resolution in the noise power measurement can be estimated using $\Delta T/T_{bg} = 1/(B\tau)^{1/2}$ as $\sim$10 ms.

Displacement detection. In the displacement measurements, we first calibrate the piezoelectric actuator disk motion amplitude using Michelson interferometry: $dz/dV \approx 0.33\ \mathrm{nm\,V^{-1}}$ at the motion frequency $f_M \approx 1$ MHz. In the RF-STM-based measurements, the displacement of the Au sample (shaken by the piezo-actuator at frequency f_M) is measured by launching an RF (carrier) signal of amplitude V_c at frequency f_{LC} towards the tank circuit, and by measuring the reflected signal amplitude V_r. A time-dependent tunnel junction resistance, $R_T(t)$, results in a time-dependent reflection coefficient, $\Gamma(t)$, which modulates the amplitude of the reflected signal. As the reflected signal is $V_r = \Gamma V_c$, we obtain reflection at f_{LC} as well as at the sidebands $f_{LC} + f_M$ and $f_{LC} - f_M$ (see Fig. 3b).

In membrane displacement measurements, the membranes are driven by a similar piezoelectric disk (Fig. 3a). The piezo-actuator drive is provided by a network analyser, which can perform frequency sweeps near the membrane resonances. The RF-STM signal at $f_{LC} + f_M$ due to the membrane motion at f_M is mixed-down with the carrier signal at f_{LC}. The IF output of the mixer is connected to the input port of the network analyser.